# NUMERICAL SIMULATIONS AND OPTIMIZATIONS FOR TURBINE-RELATED CONFIGURATIONS

by

***Jinguang YANG, Min ZHANG, and Yan LIU*****

Key Laboratory of Ocean Energy Utilization and Energy Conservation of Ministry of Education,
School of Energy and Power Engineering,
Dalian University of Technology, Dalian, Liaoning, China

Original scientific paper
https://doi.org/10.2298/TSCI190404295Y

*In order to accelerate the numerical simulation and optimization of gas turbine-related configurations, a source based computational fluid dynamics (SCFD) approach is developed for flow and heat transfer simulations. Different sources depending on the fluid porosity at each grid node in the computational domain are introduced to the continuity, momentum, energy and turbulence model equations, so that both the fluid and solid regions can be solved as one region. In the present paper, test cases including a ribbed channel and a winglet shrouded turbine cascade with tip injection are investigated using the SCFD and CFD with body-fitted meshes. Impacts of grid clustering and turbulence model equation sources on the SCFD precision are examined. Numerical results show that the SCFD predicts consistent aero-thermal performance with the fluid dynamics with body-fitted meshes and experiments. The validated SCFD scheme is then employed in a response surface optimization of tip jet holes on the winglet shroud tip. A jet arrangement with the minimum energy loss and injection mass-flow rate is obtained, indicating that source based predictions can be applied to the preliminary aero-thermal design of turbine blades.*

Key words: *SCFD, optimization, numerical simulation, turbine flow and heat transfer*

## Introduction

With the development in computer technologies and numerical algorithms, CFD has become an indispensable tool to evaluate gas turbine aero-thermal performance. Moreover, CFD-based optimization plays a crucial role in turbine design systems [1]. Various CFD methods have been proposed in the literature to model the flow and heat transfer in gas turbines. The most precise one may belong to the conjugate heat transfer (CHT) [2]. However, the high computational cost makes the CHT approach inappropriate for turbine preliminary designs [3]. Meanwhile, an essential step in the CHT procedure is to generate body-fitted meshes. This makes the grid generation process time consuming for complex turbine components especially when cooling structures [4, 5] are included.

To surmount the mentioned issues, fictitious domain (FD) methods [6, 7] are proposed. This procedure applies a relatively simple mesh to discretize a domain including any complicated structures, then it solves a single set of governing equation where penalization source terms are introduced. He and Tefti [8] applied the immerse boundary method (IBM), which is a branch of the FD scheme, to predict the flow and heat transfer in a ribbed duct. Compared to experiments and CFD simulations using body-fitted meshes, the IBM prediction

* Corresponding author, e-mail: yanliu@dlut.edu.cn

obtained generally satisfying flow and thermal properties. Moreover, an immersed mesh block (IMB) scheme, which reduced the cost of generating body-fitted meshes, was validated by Lad *et al.* [9] for cooled turbine aero-thermal performance evaluation. Andrei *et al.* [10] developed a film cooling model (FCM) for gas turbines. They declared that the FCM-based prediction has an excellent consistence in the adiabatic cooling effectiveness with measurements, and hence it can be utilized in turbine preliminary design systems.

The primary purpose of literature sources [6-10] is to avoid generating body-fitted meshes to facilitate numerical preprocessing and solution steps. Source terms are introduced to the governing equations to model multi-physical fields. This CFD approach, termed as SCFD here, is also applied as a numerical tool for objective evaluation during the topology optimization (TopOpt) [11]. The design parameter of TopOpt is the fluid porosity, $\gamma$, at each grid node in the design space. It takes values of 0 and 1, denoting the solid and fluid materials, respectively. Distributions of the $\gamma$ are gradually optimized and hence solid and fluid regions are constantly changed. In order not to update the mesh after each iteration step, the design space is generally discretized using a single set of uniform mesh and source terms depending on the $\gamma$ are introduced to the governing equation [12-14]. Though the SCFD method has been widely employed, its accuracy is not fully validated in those TopOpt investigations [11-14]. In addition, most of those TopOpt studies just penalized the momentum equation, while the turbulence model equation was not modified. This may be not adequate for the high Reynolds number turbulent flow in turbines.

In order to fix the aforementioned problem, this article establishes a SCFD procedure for turbine flow and thermal analyses. Effects of the uniform grid cell width and the turbulence model equation sources on the precision of SCFD are analyzed. Then the SCFD is combined with an optimization procedure to design tip jet holes on a winglet shrouded turbine blade. It is intended to present an efficient tool for turbine aero-thermal analysis and preliminary design systems. Meanwhile, it can also provide a theory basis for future topology optimization studies.

## Source based CFD description

### *Flow and thermal fields modeling*

Equation (1) formulates the steady-state continuity and momentum equations, where a source term, $F_\mathrm{m} = \alpha(\gamma)U$, is added to account for the resistance of solid to fluid. The Brinkman penalization factor, $\alpha(\gamma)$, varies with $\gamma$ following eq. (2), where $pe$ is a penalization coefficient. The $\alpha$ is sufficiently large ($10^5$~$10^6$) when $\gamma$ equals zero which corresponds to the solid, and this makes the velocity approach zero to satisfy the no-slip boundary condition. Meanwhile, $\alpha(\gamma)$ vanishes for the fluid material ($\gamma = 1.0$), and the classical Navier-Stokes equation can be recovered:

$$\begin{cases} \dfrac{\partial(\rho U_j)}{\partial x_j} = 0 \\ \dfrac{\partial(\rho U_i U_j)}{\partial x_j} - \dfrac{\partial}{\partial x_j}\left[(\mu+\mu_t)\left(\dfrac{\partial U_i}{\partial x_j}+\dfrac{\partial U_j}{\partial x_i}\right)\right] + \dfrac{\partial p}{\partial x_i} + \rho F_\mathrm{m} = 0 \end{cases} \tag{1}$$

Similarly, a unified energy equation is deduced to model the thermal field of the domain containing fluid and solid materials. It is presented in eq. (3), where the thermal conductivity, $\lambda(\gamma)$, and the source term, $S_\mathrm{h}$, are related to $\gamma$ *via* eq. (4). The $S_\mathrm{h}$ can make eq. (3) reduce to the fluid energy equation and the solid heat conduction equation, when $\gamma$ is 1 and 0, respectively:

$$F_{\mathrm{m}} = \alpha(\gamma) U_i, \quad \alpha(\gamma) = (1 - \gamma^{1/pe}) \alpha_{\max} \tag{2}$$

$$\gamma \frac{\partial(\rho U_j h_{\mathrm{tot}})}{\partial x_j} = \frac{\partial}{\partial x_j}\left[\lambda(\gamma)\frac{\partial T}{\partial x_j}\right] + S_{\mathrm{h}} \tag{3}$$

$$S_{\mathrm{h}} = \gamma \frac{\partial}{\partial x_j}\left(\frac{\mu_t}{\mathrm{Pr}_t}\frac{\partial h}{\partial x_j}\right), \quad \lambda(\gamma) = (1-\gamma)\lambda_S + \gamma\lambda_F \tag{4}$$

### *Turbulence modeling*

Numerical simulations are conducted using the Reynolds averaging approach, where the $k$-$\omega$ turbulence mode is used to close the equation set. Transport equations for the turbulent kinetic energy, $k$, and the specific turbulence dissipation rate, $\omega$, are formulated in eq. (5), where $\beta_k = 0.09$, $\alpha_\omega = 5/9$, $\beta_\omega = 0.075$, and $\sigma_\omega = \sigma_k = 2.0$ are the model constants [15]. Two penalization terms ($S_k$ and $S_\omega$), proposed by Dilgen *et al.* [13], are added to consider effects of the porosity, $\gamma$, on the turbulence. They ensure that near the solid material ($\gamma = 0$), $k$ approaches zero (*i. e.*, $k_S = 0$) and $\omega$ approaches $\omega_S$ due to the penalty effect of the significantly large value of $\alpha$. The $\omega_S$ represents the specific turbulence dissipation rate near the solid wall and is calculated using eq. (7) [16], where $y_1$ is the distance of the first grid cell center away from the wall. Effects of these turbulence model source terms will be discussed later:

$$\begin{cases} \dfrac{\partial}{\partial x_j}(\rho U_j k) - \dfrac{\partial}{\partial x_j}\left[\left(\mu + \dfrac{\mu_t}{\sigma_k}\right)\dfrac{\partial k}{\partial x_j}\right] - P_k + \beta_k \rho k w + P_{kb} + \rho S_k = 0 \\ \dfrac{\partial}{\partial x_j}(\rho U_j \omega) - \dfrac{\partial}{\partial x_j}\left[\left(\mu + \dfrac{\mu_t}{\sigma_\omega}\right)\dfrac{\partial \omega}{\partial x_j}\right] - a_\omega \dfrac{\omega}{k} P_k + \beta_\omega \rho w^2 + \rho S_\omega = 0 \end{cases} \tag{5}$$

$$S_k = \rho\alpha(\gamma)k, \quad S_\omega = \alpha(\gamma)(\omega - \omega_b) \tag{6}$$

$$\omega_S = \frac{60\nu}{\beta_1 y_1^2}, \quad \beta_1 = 0.075 \tag{7}$$

### *Tip injection modeling*

The injection source model in [10] is adopted to predict the influence of the tip injections on the aero-thermal performance of a linear turbine cascade in this paper. Since the jet fluid introduces extra energy into the flow field, source terms of $S_{ma,\mathrm{jet}}$, $S_{mo,\mathrm{jet}}$, and $S_{en,\mathrm{jet}}$ formulated in eq. (8) are further added in the continuity, momentum, and energy equations in eqs. (1) and (3). The mass-flow rate, $m_{\mathrm{jet}}$, volume of injection region, $Vol_{\mathrm{jet}}$, velocity, $u_{\mathrm{jet,I}}$, and internal energy, $e_{\mathrm{jet}}$, associated with the jet stream need to be specified prior to simulations:

$$\begin{cases} S_{ma,\mathrm{jet}} = \dfrac{m_{\mathrm{jet}}}{Vol_{\mathrm{jet}}} \\ S_{mo,\mathrm{jet}} = S_{ma,\mathrm{jet}} \cdot u_{\mathrm{jet},i} \\ S_{en,\mathrm{jet}} = S_{ma,\mathrm{jet}}(e_{\mathrm{jet}} + 0.5u_{\mathrm{jet},i}^2), e_{\mathrm{jet}} = (c_{\mathrm{p}} - R)T_{\mathrm{jet}} \end{cases} \tag{8}$$

## The SCFD validation

Numerical simulations of typical turbine flow and heat transfer cases are performed using the ANSYS CFX software to validate the SCFD method. All source terms are implemented via CFX User Fortran functions [17]. Special comments will be made on the grid generation scheme. Effects of the turbulence model equation sources, *i. e.* $S_k$ and $S_\omega$ in eq. (7), are also evaluated.

### *Rib channel flow and heat transfer*

Rib geometries are generally employed to augment the turbine blade heat transfer. A 2-D computational domain for the ribbed duct tested by Archarya *et al.* [18] is shown in fig. 1, where $\Omega_{\text{in}}$ and $\Omega_{\text{rib}}$ represent an upstream domain and the rib region domain, respectively. The length ($L$) and height ($H$) of the $\Omega_{\text{rib}}$ are the same to that of the experimental configuration. The Reynolds number based on the bulk velocity, $U_{\text{b}}$, and channel hydraulic diameter, $D_{\text{h}}$, is $2.4\times10^4$. Eight square balsa-wood ribs with a height of $e$ are uniformly distributed on the bottom wall. The rib pitch, $P$, is about $20e$. Numerical simulations are conducted using the CFD with body-fitted meshes (BCFD) and the SCFD, respectively. For the BCFD approach, solid rib regions are not meshed and a body-fitted mesh is generated. For the SCFD scheme, the computational domain includes eight solid rib regions and a uniform mesh (UM) is created. Moreover, in order to investigate the impact of $S_k$ and $S_\omega$ in eq. (5), the SCFD is further divided into SCFD-P and SCFD-T, which denote the SCFD scheme without and with penalization terms in the turbulence model equations, respectively.

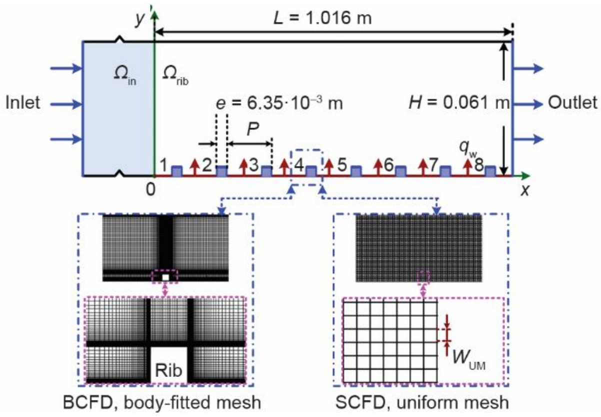


**Figure 1. Computational domain and details of the mesh near the rib**

For all BCFD and SCFD simulations, a normal velocity with a medium turbulence intensity (5%) is specified at the inlet. The inlet static temperature and outlet pressure are also defined. According to the experimental conditions [18], a heat flux, $q_{\text{w}}$, is only defined on the bottom wall, while all other walls including the rib surfaces are adiabatic. The convective heat transfer coefficient, $h$, and the Nusselt number are calculated using eq. (9), where the bulk temperature, $T_{\text{b}}$, is defined as the mass averaged temperature over each stream-wise plane [18]:

$$h = \frac{q_w}{\Delta T}, \quad \text{Nu} = \frac{hL}{k_{\text{f}}}, \quad \Delta T = T_w - T_{\text{b}} \tag{9}$$

In order to examine the grid independence for the SCFD scheme, three values of the grid cell width being $W_{\mathrm{UM},1} = e/60$, $W_{\mathrm{UM},2} = e/40$, and $W_{\mathrm{UM},3} = e/20$ are used to generate the uniform meshes, they correspond to the total number of grid cells being $N_1$ = 5.53 million, $N_2$ = 2.32 million, and $N_3$ = 0.61 million, respectively. The cell numbers lead to a grid refinement factor $r_{31}$ of about 3.0, which satisfies a requirement of being greater than 1.3 [19]. For these three sets of grids, discretization errors of the SCFD are listed in tab. 1, where examined parameters, $\varphi$, include the total pressure loss coefficient at the outlet, $C_{pt,\mathrm{out}}$, and the Nusselt number at the location 0.6$P$ downstream of rib 6, respectively. Definition of the $C_{pt}$ is given in eq. (10) and process of calculating the grid convergence index (GCI) values can be referred to [19]. It is seen from tab. 1 that numerical uncertainties in both coarse-grid and fine-grid solutions ($\mathrm{GCI}^{32}$ and $\mathrm{GCI}^{21}$) for $C_{pt,\mathrm{out}}$ are sufficiently small, while those for $\mathrm{Nu}_{0.6}$ are relatively large. So the SCFD-T-UM predicts the flow field well for all three values of the $W_{\mathrm{UM}}$, but it has less accuracy in modeling thermal properties. Reasons for this result will be discussed later.

**Table 1. Calculations of the discretization error**

| Parameters | | Value | | Parameters | | Value | |
|---|---|---|---|---|---|---|---|
| | | $C_{pt,\mathrm{out}}$ | $\mathrm{Nu}_{0.6}$ | | | $C_{pt,\mathrm{out}}$ | $\mathrm{Nu}_{0.6}$ |
| Grid refinement factors | $r_{21}$ | 1.5 | 1.5 | Approximate relative error | $e_{\mathrm{a}}^{21}$ | 0.370% | 4.202% |
| | $r_{32}$ | 2.0 | 2.0 | | $e_{\mathrm{a}}^{32}$ | 2.292% | 28.130% |
| Computed parameters ($\varphi = C_{pt}$ or $\mathrm{Nu}_{0.6}$) | $\varphi_1$ | 0.354 | 57.838 | Extrapolated relative error | $e_{\mathrm{ext}}^{21}$ | 0.253% | 2.680% |
| | $\varphi_2$ | 0.353 | 55.408 | | $e_{\mathrm{ext}}^{32}$ | 0.622% | 6.769% |
| | $\varphi_3$ | 0.345 | 39.821 | Grid convergence index | $\mathrm{GCI}^{21}$ | 0.317% | 3.442% |
| Extrapolated values | $\varphi_{\mathrm{ext}}^{21}$ | 0.355 | 59.431 | | $\mathrm{GCI}^{32}$ | 0.782% | 9.076% |
| | $\varphi_{\mathrm{ext}}^{32}$ | 0.354 | 59.430 | | | | |

$$C_{pt} = \frac{P_{\mathrm{t,in}} - P_{\mathrm{t}}}{P_{\mathrm{t,in}} - P_{\mathrm{s,out}}} \tag{10}$$

With the coarse, medium and fine uniform meshes examined in tab. 1, SCFD-P simulations are then conducted. Meanwhile, a BCFD prediction is performed after another GCI study, which is not presented here for simplicity. Figures 2 and 3 compare flow fields and Nusselt number on the bottom wall across one pitch, $P$, region around rib 6, respectively. Compared to the BCFD in fig. 2(a), the SCFD-P under-predicts flow separations near the rib, as shown in figs. 2(b) and 2(c). Kang and Yang [20] noted that the heat transfer on the ribbed-duct wall is related to the vortex size. Smaller size vortex transports less cold main-stream fluid to the heated wall, so the wall temperature, $T_{\mathrm{w}}$, in SCFD-P predictions is higher than that in BCFD case. According to eq. (9), higher $T_{\mathrm{w}}$ results in lower wall temperature drop, $\Delta T$, and hence larger $h$ and Nusselt number. Therefore, the SCFD-P over-predicts the Nusselt number, as shown in fig. 3. These imply that neglecting the turbulence model equation sources cannot get accurate SCFD results.

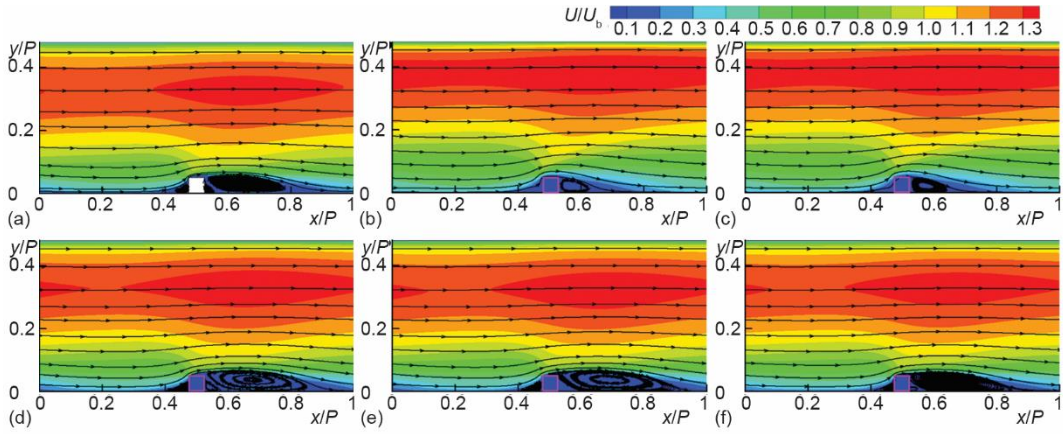


**Figure 2. Contours of normalized velocity and flow streamlines near the rib 6; (a) BCFD, (b) SCFD-P,$W_{UM,2}$, (c) SCFD-P,$W_{UM,1}$, (d) SCFD-T,$W_{UM,3}$, (e) SCFD-T,$W_{UM,2}$, (f) SCFD-T,$W_{UM,1}$**

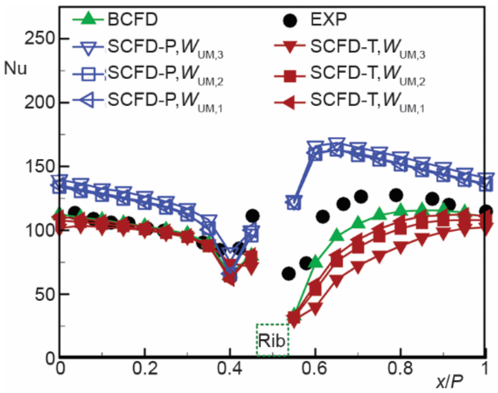


**Figure 3. Distribution of Nusselt number on the bottom wall across one pitch (P) region of the rib channel**

Figures 2(d)-2(f) indicate that small discrepancies exist in flow properties among the SCFD-T predictions. This validates the GCI study for the $C_{pt,\mathrm{out}}$. However, there are differences in Nusselt number among the SCFD-T predictions, especially in regions downstream the rib ($x/P > 0.55$) in fig. 3. To interprete the reason for this accurate flow data but inaccurate Nusselt number, BCFD, and SCFD-T, predicted $T_w$ and $T_b$ are compared. It is observed that the difference in $T_w$ is just 1 K between the SCFD-T-$W_{UM,3}$ and BCFD, while the $T_b$ is almost the same between them. As signified by Baughn *et al.* [21], small differences in the $\Delta T$ could lead to large uncertainties in Nusselt numbers, especially at high heat flux. So errors in Nusselt number for the SCFD-T-$W_{UM,3}$ are ascribed to incorrect $T_w$. However, discrepancies in Nu between the SCFD-T and the BCFD become small when $W_{UM}$ equals $W_{UM,1}$. These analyses demonstrate that the uniform mesh is feasible for SCFD simulations, and its grid cell width has critical impacts on the heat transfer but little effects on the flow fields.

### *Aerodynamic performance of a winglet shroud tip with tip injection*

The authors [22] have designed a winglet-shroud (WS) tip to control the tip leakage flow for a linear turbine cascade, and conducted experiments and BCFD simulations to evaluate the aerodynamic performance of the WS tip with tip injections. Figure 4 illustrates the experimental WS tip geometry with five circular jet holes. Detailed information is described in the previous paper [23]. These tip jet cases are re-examined here using injection source models to further validate the SCFD procedure. The computational domain is also shown in fig. 4.

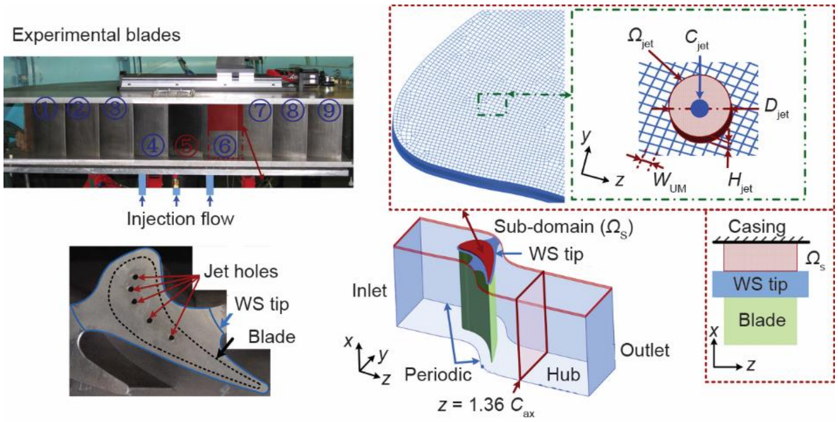


**Figure 4. Computational domain**

The injection flow passages are not constructed in the SCFD predictions. To model the tip injection flow, a sub-domain, $\Omega_S$, is created above the blade tip and five injection volumes, $\Omega_{jet}$, shown in fig. 4 can be defined. The $\Omega_{jet}$ is a circular cylinder with a diameter of $D_{jet}$ and a height of $H_{jet}$ being 0.05 $D_{jet}$. The center of the cylinder bottom section coincides with that of jet holes, $C_{jet}$. During the SCFD simulation, injection source terms, defined in eq. (8), are introduced at grid nodes contained in $\Omega_{jet}$ regions. Identification of the $\Omega_{jet}$ and source grid nodes are realized using the CFX User Fortran code based on the coordinate information. In addition, the porosity of the grid nodes on the solid wall, which is the interface between $\Omega_S$ and WS tip region, should be defined as zero to introduce penalizations terms in eqs. (1)-(5).

The number of grid nodes is about 8 million according to a previous GCI study [23]. The $\Omega_S$ is discretized using nearly uniform meshes when seeing the surface grid in $y$-$z$ plane. The grid cell width, $W_{UM}$, is about one eighth of the $D_{jet}$ according to a grid independence study and the recommendation of Andrei *et al.* [10]. Measured total pressure, $P_{t,in}$, and temperature, $T_{t,in}$, are set at the inlet, where a flow angle of 37.5° is also specified. A static pressure, $P_{s,out}$, tested in the experiment is defined at the outlet. The energy loss coefficient, $\xi$, previously deduced [23] is applied for performance evaluation, and its definition is given in eq. (11), where $P_{t,ave}$ denotes a work-average total pressure and temperature:

$$\xi = \frac{\left(\dfrac{P_s}{P_t}\right)^{(k-1)/k} - \left(\dfrac{P_s}{P_{t,ave}}\right)^{(k-1)/k}}{1-\left(\dfrac{P_s}{P_{t,ave}}\right)^{(k-1)/k}} \tag{11}$$

Contours of $\xi$ and secondary flow streamlines on the 1.36$C_{ax}$ plane are displayed in fig. 5, where color in regions with $\xi$ below 0.1 is cut off from the contour map for clarity. The mass averaged $\xi$ over the 1.36$C_{ax}$ plane ($\xi_m$) against the injection mass ratio is plotted in fig. 6. Experiments did not capture the upper passage vortex (UPV) due to weak UPV intensity and sparse testing points in this region [23], while the SCFD prediction obtains similar UPV and tip leakage vortex (TLV) structures to the BCFD. The profile loss ($\xi$ value in the region around $y/p$ being 0.5) in fig. 5(c) is larger than that in figs. 5(a) and 5(b). This is because the SCFD cannot consider the flow resistance in the blade internal jet passage, hence it gets higher jet flow velocity and more intense diffusion of low-energy fluid. Despite this error, the SCFD predicted $\xi_m$ has the same varying trend in fig. 6 as the BCFD data. This implies that the SCFD is appropriate to estimate the impact of tip injections on the blade aerodynamic performance.

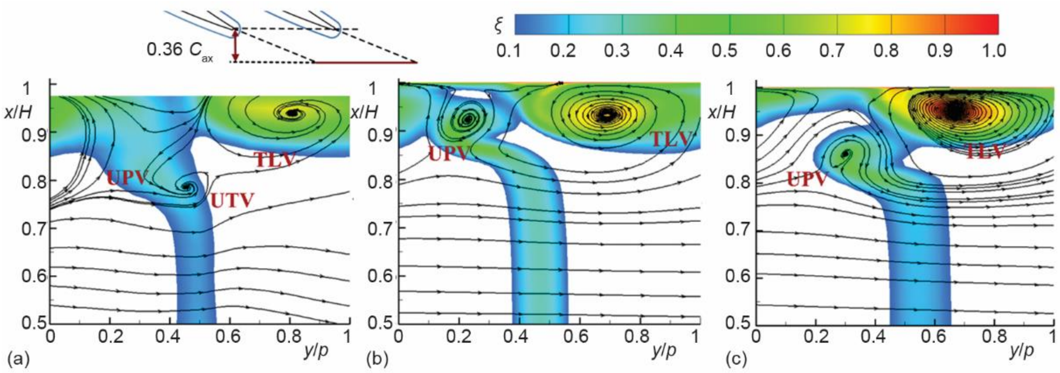


**Figure 5. Flow patterns on the 1.36$C_{ax}$ plane, $M_{r,jet}$ = 0.5%; (a) EXP, (b) BCFD, (c) SCFD**

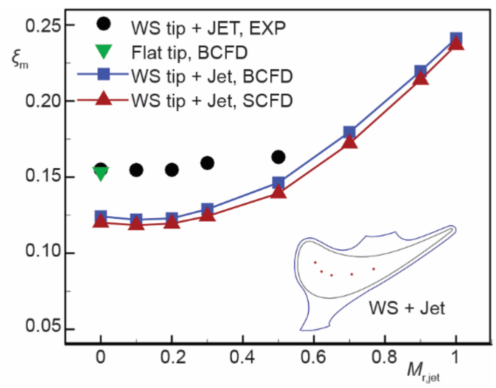


**Figure 6. Mass-averaged $\xi$ over upper half area of 1.36$C_{ax}$ plane**

## The SCFD application in a tip jet hole optimization scheme

The previous section validates the source model prediction for turbine flow and heat transfer analysis, while this section further extends the SCFD to an optimization scheme for designing tip jet holes for the cascade in fig. 4.

### *Jet hole optimization problem*

Equation (12) delineates the mathematic formulation for the optimization. The objective is to obtain a jet hole configuration with the minimum energy loss, $\xi$, under the least injection mass flow rate, $m_{jet}$, while the design variable vector, $\boldsymbol{\chi}$, includes number, $N_{jet}$, and radius, $R_{jet}$, of circular jet holes, ratio, $M_{r,jet}$, of jet mass-flow rate to main stream mass-flow rate and a distance ratio, $D_{r,PS}$. The $N_{jet}$ takes discrete value and the other variables are continuous, and value ranges for $R_{jet}$ and $M_{r,jet}$ are defined based on engine-realistic conditions [24].

The parameter $D_{r,PS}$ is the ratio of distance between the hole center and the pressure surface, $D_{jet,PS}$, to the blade thickness, $\delta_{jet}$. It is used to explicitly locate each hole center and is constant for all holes. The holes are equally arranged in the axial direction ($z$-axis), as illustrated in fig. 7. The space between a hole and its adjacent one is $(z_{jet,max} - z_{jet,min})/N_{jet}$, where $z_{jet,min}$ and $z_{jet,max}$ are two specified values to limit the axial location of jet holes. Pressure and suction side profiles of the blade are simply fitted using polynomials as described by $y_{max}(z)$ and $y_{min}(z)$, respectively, and coordinates of the $i^{th}$ hole center, $C_{jet,I}$, are determined using eq. (13).

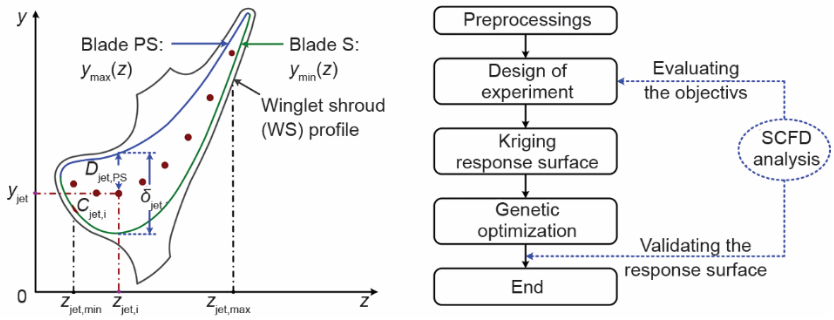


**Figure 7. Definition for the jet holes and the optimization flow-chart**

### *Optimization method*

Solution for the optimization problem in eq. (12) is realized using a response surface (RS) optimization scheme in ANSYS WORKBENCH, and the whole flow chart is also given in fig. 7. A design of experiment (DOE) analysis is first executed for design samplings, which are produced here using the optimal space filling (OSF) method based on the design space. Then Kriging RS, which formulate design objectives in terms of each design parameter, are generated. Information drawn from the RS evaluation is finally utilized by a multi-objective genetic algorithm solver. The optimization is converged after 11 iterations and 500 samples are evaluated at each iteration step. Then three design candidates or Pareto optimum results are produced. Since the interpolated RS significantly affects the optimization precision, its quality will be validated after the optimization. It is worth mentioning that the SCFD method is used in the DOE part to evaluate the objective for each design sampling.

$$\begin{aligned}&\text{min.}\ \begin{cases}\xi(\chi)\\ m_{\text{jet}}(\chi)\end{cases},\ \chi=\left[N_{\text{jet}},\ R_{\text{jet}},\ M_{\text{r,jet}},\ D_{\text{r,PS}}\right]\\ &\text{s.t.}\ \begin{cases}N_{\text{jet}} & \in\{6,7,8,\cdots\cdots\cdots 20\}\\ R_{\text{jet}} & \in[1.0\text{ mm},\ 2.0\text{ mm}]\\ M_{\text{r,jet}} & \in[0.5\%,\ 2.0\%]\\ D_{\text{r,PS}} & \in[0.25,\ 0.75]\end{cases}\end{aligned} \tag{12}$$

$$\begin{cases}z_{\text{jet},i} = z_{\text{jet,min}}+\dfrac{z_{\text{jet,max}}-z_{\text{jet,min}}}{N_{\text{hole}}-1}i_{\text{hole}}, & i=\{1,2,\cdots N_{\text{hole}}\}\\ y_{\text{jet},i} = y_{\text{min}}(z_{\text{jet,i}})+\left[y_{\text{max}}(z_{\text{jet},i})-y_{\text{min}}(z_{\text{jet},i})\right]D_{\text{r,PS}}\end{cases} \tag{13}$$

### *Optimization results*

A trade off diagram between the two design objectives, *i. e.*, the injection mass-flow rate, $m_{\text{jet}}$, and the energy loss coefficient, $\xi$, is shown in fig. 8, where one can determine feasible and infeasible solutions. Optimization samples are ranked by different Pareto fronts, the lower the Pareto front number (Pareto 1-3), the better the performance of design samples. Three de-

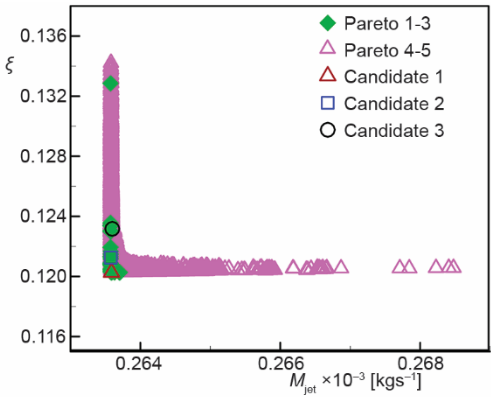


**Figure 8. Trade-off chart of the optimization**

sign candidates, also termed as Pareto-dominant solutions, are also presented in fig. 8. Their respective values of design parameters are subsequently used in simulations with the SCFD scheme for performance validation.

Table 2 lists the objective data of each candidate design. The subscripts RS and CFD in the $\xi$ and $m_{jet}$ represent values obtained by the RS and predicted by the SCFD scheme, respectively. Small discrepancies in $\xi$ and $M_{r,jet}$ between RS and SCFD results confirm the good quality of response surfaces created from DOE part and employed in MOGA step. Under the similar $m_{jet}$ of 0.0026 kg/s, which corresponds to $M_{r,jet}$ being 0.5% in fig. 8, the energy loss coefficient is decreased by 13.78%, 13.57%, and 13.64% for the three candidate designs compared to the jet configuration in section *Aerodynamic performance of a winglet shroud tip with tip injection*. Detailed flow fields in these designs need to be investigated using the BCFD in future, while this result proves the effectiveness of the present optimization and demonstrates the potential of the SCFD in turbine preliminary aero-thermal design process.

**Table 2. Candidate points for the optimization**

| Cases | Design parameters | | | | Objectives | | | |
|---|---|---|---|---|---|---|---|---|
| | $M_{r,jet}$ | $D_{r,PS}$ | $N_{jet}$ | $R_{jet}$ [mm] | $\xi_{RS}$ | $\xi_{CFD}$ | $m_{jet,RS}$ [kgs$^{-1}$] | $m_{jet,CFD}$ [kgs$^{-1}$] |
| 1 | 0.005 | 0.2884 | 19 | 2 | 0.1233 | 0.1262 | 0.0026 | 0.0026 |
| 2 | 0.005 | 0.7846 | 5 | 1.4 | 0.1254 | 0.1265 | 0.0026 | 0.0026 |
| 3 | 0.005 | 0.7796 | 7 | 2 | 0.1218 | 0.1264 | 0.0026 | 0.0026 |

## Conclusions

A SCFD method has been summarized in this paper to realize aero-thermal analyses using a single set of mesh. Flow and heat transfer properties in a ribbed duct and effects of tip injections on the aerodynamic performance for a turbine winglet shroud tip are simulated for model validation. The SCFD scheme is finally combined with a optimization procedure to design jet configurations on the winglet shroud tip. Some conclusions are listed as follow.

- For the ribbed channel case, the turbulence model equation sources improve the accuracy of SCFD predictions in simulating flow and thermal properties. The SCFD precision can also be guaranteed using uniform meshes with an adequate cell width. Meanwhile, lowering the uniform grid cell width has slight effects on the flow characteristics but has critical impacts on the heat transfer data.
- The SCFD captures major vortex structures in the winglet-shrouded turbine cascade. Varying trends of the energy loss with injection ratios predicted by the SCFD agree well with those by CFD using body-fitted meshes. Therefore, the SCFD strategy can be applied for estimating the aerodynamic performance of the turbine blade tip injection.

- Three design candidates, also termed as Pareto-dominant solutions, for jet holes with the minimal loss and injection mass flow rates are achieved. Under the similar injection mass-flow rate, the energy loss is decreased by 13.78%, 13.57%, and 13.64%, respectively for these candidates compared to the original jet arrangement. This offers a verification of the SCFD approach to be employed as a tool for performance evaluation in turbine preliminary aero-thermal design systems.

**Acknowledgment**

The authors would like to thank the National Natural Science Foundation of China (NSFC, Grant No.51606026 and 51876021) for funding this work.

## Nomenclature

$C_p$ – specific heat at constant pressure, [$Jkg^{-1}K^{-1}$]
$C_{pt}$ – total pressure loss coefficient, [–]
$D_{jet}$ – jet hole diameter = 2.0 $R_{jet}$, [m]
$e$ – rib height, [m]
$e_{jet}$ – internal energy of jet flow
$\mathbf{F_m}$ – momentum equation source term
$h$ – heat transfer coefficient, [$Wm^{-2}K^{-1}$]
$h_{tot}$ – total enthalpy, [$Jkg^{-1}$]
$H$ – height of the $\Omega_{rib}$, [m]
$H_{jet}$ – height of the $\Omega_{jet}$, [m]
$k$ – turbulence kinetic energy, [$m^2s^{-2}$]
$L$ – length of the $\Omega_{rib}$, [m]
$m_{in}$ – main stream mass flow rate, [$kgs^{-1}$]
$m_{jet}$ – tip injection mass flow rate, [$kgs^{-1}$]
$M_{r,jet}$ – injection ratio of $m_{jet}$ to $m_{in}$, [–]
$N_{jet}$ – jet hole number
Nu – Nusselt number, [–]
$P$ – rib channel pitch, [m]
$pe$ – penalization coefficient, [–]
$P_s$ – static pressure, [Pa]
$P_t$ – total pressure, [Pa]
$P_{t,\ ave}$ – work-average total pressure
$q_w$ – wall heat flux, [$Wm^{-2}$]
R – gas constant [$Jkg^{-1}K^{-1}$]
$S_h$ – energy equation source term
$S_{ma,jet}$ – continuity equation source of jet flow
$S_{mo,jet}$ – momentum equation source of jet flow
$S_{en,jet}$ – energy equation source of jet flow
$T_b$ – bulk temperature, [K]
$T_t$ – total temperature, [K]
$T_w$ – wall temperature, [K]
$U_j$ – velocity, [$ms^{-1}$]
$u_{jet,i}$ – jet flow velocity, [$ms^{-1}$]
$Vol_{jet}$ – volume of the $\Omega_{jet}$, [$m^3$]
$W_{UM}$ – grid cell width of uniform meshes, [m]

*Greek symbols*

$\alpha$ – brinkman penalization factor, [$kgm^{-3}s^{-1}$]
$\xi$ – energy loss coefficient, [–]
$\gamma$ – fluid porosity, [–]
$\lambda$ – thermal conductivity, [$Wm^{-1}K$]
$\mu$ – dynamic viscosity, [Pa·s]
$\mu_t$ – turbulence viscosity, [Pa·s]
$\rho$ – density, [$kgm^{-3}$]
$\nu$ – kinematic viscosity, [$m^2s^{-1}$]
$\chi$ – design variable vector, [–]
$\omega$ – specific turbulence dissipation rate, [$s^{-1}$]
$\Omega_{in}$ – upstream domain of the rib channel, [–]
$\Omega_{jet}$ – injection volumes, [–]
$\Omega_{rib}$ – rib channel domain, [–]
$\Omega_S$ – sub-domain for injection source, [–]

*Acronyms*

BCFD – CFD using body-fitted mesh
BM – body-fitted mesh
CHT – conjugate heat transfer
DOE – design of experiment
EXP – experiments
FCM – film cooling model
FD – fictitious domain
GCI – grid convergence index
IBM – immerse boundary method
MOGA – multi-objective genetic algorithm
OSF – optimal space filling
RS – response surface
SCFD – source based CFD
SCFD-P – SCFD without turbulence model equation source
SCFD-T – SCFD with turbulence model equation source
TLV – tip leakage vortex
UM – uniform meshes
UPV – upper passage vortex
WS – winglet shroud

## References

[1] Johnson, G. J. J., *et al*., Design Optimization Methods for Improving HPT Vane Pressure Side Cooling Properties Using Genetic Algorithms and Efficient CFD, Report No. AIAA 2012-0326, Nashville, Tenn., USA, 2012.
[2] Amaral, S., *et al*., Design and Optimization of the Internal Cooling Channels of High Pressure Turbine Blade, Part I, Methodology, *J. Turbomach.*, *132* (2010), 2, ID 021013
[3] Maffulli, R., He, L., Wall Temperature Effects on Heat Transfer Coefficient for High-Pressure Turbines, *J. Propul. Power*, *30* (2014), 4, pp.1080-1090
[4] Ravi, D., Parammasivam, K. M., Enhancing Film Cooling Effectiveness in a Gas Turbine End-Wall with a Passive Semi Cylindrical, *Thermal Science, 23* (2019), 3, pp. 2013-2023
[5] Xie, Y. H., *et al*., Numerical Study on Film Cooling and Convective Heat Transfer Characteristics in the Cutback Region of Turbine Blade Trailing Edge, *Thermal Science, 20* (2016), Suppl. 3, S643-S649
[6] Khadra, K., *et al*., Fictitious Domain Approach for Numerical Modeling of Navier-Stokes Equations, *Int. J. Numer. Methods Fluids*, *34* (2000), 8, pp. 651-684
[7] Wang, Y. L., Shao, X. M., Study on Flow of Power-Law Fluid Through an Infinite Array of Circular Cylinders with Immersed Boundary-Lattice Boltzmann Method, *Thermal Science, 16* (2012), 5, pp. 1451-1455
[8] He, L., Tafti, D., Evaluating the Immersed Boundary Method in a Ribbed Duct for the Internal Cooling of Turbine Blades, Report No. ASME GT2015-43953, Montreal, Canada, 2015
[9] Lad, B., *et al*., Validation of the Immersed Mesh Block (IMB) Approach Against a Cooled Transonic Turbine Stage, Report No. Report No. GT2012-68779, Copenhagen, Denmark, 2012
[10] Andrei, L., *et al*., Film Cooling Modeling for Gas Turbine Nozzles and Blades, Validation and Application, *J. Turbomach., 139* (2016), 1, ID 011004
[11] Dbouk, T., A Review about the Engineering Design of Optimal Heat Transfer Systems Using Topology Optimization, *Appl. Therm. Eng.*, *112* (2017), Feb., pp. 841-854
[12] Pietropaoli, M., *et al*., Design for Additive Manufacturing, Internal Channel Optimization, Report No. ASME GT2016-57318, Seoul, South Korea, 2016
[13] Dilgen, C. B., *et al*., Topology Optimization of Turbulent Flow, *Comput. Methods Appl. Mech. Engrg.*, *331* (2018), Apr., pp. 363-393
[14] Iseler, J., Martin, T. J., Flow Topology Optimization of a Cooling Passage for a High Pressure Turbine Blade, Report No. ASME G2017-63618, Charlotte, USA, 2017
[15] Wilcox, D. C., Multiscale Model for Turbulent Flows, *AIAA J.*, *26* (1988), 11, pp. 1311-1320
[16] Menter, F. R., Two-Equation Eddy-Viscosity Turbulence Models for Engineering Applications, *AIAA J.*, *32* (1994), 8, pp. 1598-1605
[17] *** Ansys, Inc., *ANSYS CFX-Solver Modeling Guide*, ANSYS, Inc., Canonsburg, USA, 2013
[18] Acharya, S., *et al*., Heat Transfer in Turbulent Flow Past a Surface-Mounted Two-Dimensional Rib, *J. Heat Transfer*, *120* (1998), 3, pp. 724-734
[19] Celik, I. B., *et al*., Procedure for Estimation and Reporting of Uncertainty Due to Discretization in CFD Applications, *J. Fluids Eng.*, *130* (2008), 7, ID 078001
[20] Kang, C., Yang, K. S., Heat Transfer Enhancement in Turbulent Ribbed-Pipe Flow, *J. Heat Transfer*, *139* (2017), 7, ID 071901
[21] Baughn, J. W., *et al*., Local Heat Transfer Downstream of an Abrupt Expansion in a Circular Channel with Constant Wall Heat Flux, *J. Turbomach.*, *106* (1984), 4, pp. 789-796
[22] Liu, Y., *et al*., Numerical and Experimental Investigation of Aerodynamic Performance for a Straight Turbine Cascade with a Novel Partial Shroud, *J. Fluids Eng.*, *138* (2015), 3, ID 031206
[23] Zhang, M., *et al*., Aerodynamic Performance of Tip Injections for a Winglet-Shrouded Linear Turbine Cascade, Report No. ASME GT2017-63679, Charlotte, USA, 2017
[24] Han, J. C., Fundamental Gas Turbine Heat Transfer, *J. Therm. Sci. Eng. Appl.*, *5* (2013), 2, ID 021007

Paper submitted: April 4, 2019
Paper revised: June 11, 2019
Paper accepted: June 13, 2019